5-1-2019

Variability in X-ray Line Ratios in Helium-Like Ions of Massive Stars: The Wind-Driven Case

Richard Ignace
East Tennessee State University, ignace@etsu.edu

Z. Damrau
East Tennessee State University

K. T. Hole
Norwich University

Citation Information

Ignace, Richard; Damrau, Z.; and Hole, K. T.. 2019. Variability in X-ray Line Ratios in Helium-Like Ions of Massive Stars: The Wind-Driven Case. *Astronomy & Astrophysics*. Vol.625 https://doi.org/10.1051/0004-6361/201834752 ISSN: 0004-6361

Variability in X-ray Line Ratios in Helium-Like Ions of Massive Stars: The Wind-Driven Case

A&A 625, A86 (2019)
https://doi.org/10.1051/0004-6361/201834752

Astronomy & Astrophysics

Variability in X-ray line ratios in helium-like ions of massive stars: the wind-driven case

R. Ignace[1], Z. Damrau[1], and K. T. Hole[2]

[1] Department of Physics & Astronomy, East Tennessee State University, Johnson City, TN 37614, USA
e-mail: ignace@etsu.edu
[2] Norwich University, 158 Harmon Drive, Northfield, VT 05663, USA

Received 30 November 2018 / Accepted 13 March 2019

ABSTRACT

Context. High spectral resolution and long exposure times are providing unprecedented levels of data quality of massive stars at X-ray wavelengths.

Aims. A key diagnostic of the X-ray emitting plasma are the *fir* lines for He-like triplets. In particular, owing to radiative pumping effects, the forbidden-to-intercombination line luminosity ratio, $R = f/i$, can be used to determine the proximity of the hot plasma to the UV-bright photospheres of massive stars. Moreover, the era of large observing programs additionally allows for investigation of line variability.

Methods. This contribution is the second to explore how variability in the line ratio can provide new diagnostic information about distributed X-rays in a massive star wind. We focus on wind integration for total line luminosities, taking account of radiative pumping and stellar occultation. While the case of a variable stellar radiation field was explored in the first paper, the effects of wind variability are emphasized in this work.

Results. We formulate an expression for the ratio of line luminosities f/i that closely resembles the classic expression for the on-the-spot result. While there are many ways to drive variability in the line ratio, we use variable mass loss as an illustrative example for wind integration, particularly since this produces no variability for the on-the-spot case. The f/i ratio can be significantly modulated owing to evolving wind properties. The extent of the variation depends on how the timescale for the wind flow compares to the timescale over which the line emissivities change.

Conclusions. While a variety of factors can ellicit variable line ratios, a time-varying mass-loss rate serves to demonstrate the range of amplitude and phased-dependent behavior in f/i line ratios. Importantly, we evaluate how variable mass loss might bias measures of f/i. For observational exposures that are less than the timescale of variable mass loss, biased measures (relative to the time-averaged wind) can result; if exposures are long, the f/i ratio is reflective of the time-averaged spherical wind.

Key words. stars: early-type – stars: massive – stars: mass-loss – stars: winds, outflows – X-rays: stars

1. Introduction

While our understanding of massive star evolution and the nature of their stellar winds has advanced tremendously over recent decades, the advances have themselves generated a swath of new and challenging questions. Mass remains the foremost parameter for determining the destiny of a star (Langer 2012). Thus, aside from the many variations that can arise from mass transfer in binary stars (e.g., Vanbeveren et al. 1998; Sana et al. 2012; Postnov & Yungelson 2014), mass loss can substantially impact the story line of massive stars (e.g., Puls et al. 2008; Smith 2014).

The most successful theory for wind driving among early-type massive stars – O stars, early B stars, evolved OB stars, and even the Wolf-Rayet stars – is line-driven wind theory (Castor et al. 1975; Pauldrach et al. 1986; Friend & Abbott 1986; Lucy & Abbott 1993; Springmann 1994; Gayley 1995; Gayley et al. 1995). At the same time, this mechanism also predicts wind instabilities (i.e., the line-driven instability mechanism; hereafter LDI) that lead to the development of shocks and structured flow (Lucy & Solomon 1970; Lucy & White 1980; Owocki et al. 1988; Feldmeier et al. 1997). While LDI is a natural source of structure formation in the wind, it is also possible that convective processes initiate structure formation at the wind base (Cantiello et al. 2009; Aerts & Rogers 2015), without precluding operation of LDI. Observational support for stochastically structured flow comes in a variety of forms, including (but not limited to) the black troughs of ultraviolet (UV) P Cygni resonance lines (Lucy 1983; Prinja et al. 1990), wind clumping (e.g., Hillier 1991; Robert 1992; Eversberg et al. 1998; Blomme et al. 2003; Fullerton et al. 2006; Puls et al. 2006, 2008), and of particular interest for this paper the production of X-ray emissions in the wind (e.g., Harnden et al. 1979; Cassinelli et al. 1981; Berghoefer et al. 1997; Skinner et al. 2006; Oskinova et al. 2006; Nazé 2009).

The ability of *Chandra* and *XMM-Newton* to provide high spectral resolution studies of massive star winds has been a major contributor to further understanding the wind structure (e.g., Oskinova et al. 2007; Güdel & Nazé 2009; Leutenegger et al. 2013). Emission profile shapes of X-ray lines directly probe the kinematics of the wind flow (Ignace 2001, 2016; Owocki & Cohen 2001, 2006; Ignace & Gayley 2002; Feldmeier et al. 2003) and can be used to infer mass-loss rates, $\dot{M}$ (e.g., Cohen et al. 2014). High-resolution spectra have also been able to resolve, either separately or as partial blends, the triplet components of He-like species, such as C V, N VI, O VII, Ne IX, and others (e.g., Waldron & Cassinelli 2007). The three components are referenced as *fir* lines, which stands for forbidden, intercombination, and resonance. These lines are important because of their diagnostic ability (e.g., Porquet et al. 2001).

Of chief interest for this paper is the ratio of line luminosities $R = f/i$.

This line luminosity ratio has a predicted value based on atomic physics and has different ratio values for different elements. However, the value can be modified by pumping effects. One effect comes from collisional excitation of the forbidden line that depopulates that level in favor of the intercombination line (Gabriel & Jordan 1969). Consequently, for hot plasmas of sufficient density, the line ratio becomes a diagnostic of the density conditions. The densities in massive star winds generally have collisional pumping that is too low to be relevant (for an exception, see Oskinova et al. 2017). A second process that can change the line ratio is radiative pumping by UV photons (Blumenthal et al. 1972). Since massive stars have strong UV stellar radiation fields, and since the mean intensity of the radiation is a function of distance from the star (owing to the dilution factor), observed line ratios of f/i become diagnostics for the vicinity of X-ray producing hot plasma in relation to the stellar atmosphere (early applications of this diagnostic for massive stars included Kahn et al. 2001; Cassinelli et al. 2001). The first O supergiant study with *Chandra* High Energy Transmission Grating data demonstrated the importance of the f/i ratios as a method to establish radial locations in the stellar wind where He-like emission lines form (Waldron & Cassinelli 2001).

Several papers have explored the influence of strong stellar radiation fields on f/i line ratios. Early applications made use of an "on-the-spot" approximation, whereby the X-rays are considered to be produced in a shell so that an observed line ratio could be associated with a single radius in the wind. Optically thin X-ray emission from line cooling is a density-squared process, which is steep in the accelerating portion of the winds, so the assumption that the X-ray source is dominated by a radially thin shell is a reasonable zeroth order approximation. However, the lines are actually formed over some radial span in the wind, and this is generally different in a non-negligible way from the thin shell case. Integration over the wind is typically model-dependent (e.g., the temperature structure that determines where lines form, the volume filling factor of the plasma). Leutenegger et al. (2006) also found that overlapping and wind-broadened lines can influence the strength of the radiative pumping.

Whether through a shell or wind integration model, work has been devoted mainly toward understanding line ratios that are not time-dependent, but there are ways in which the observed ratio can become time-dependent. For example, binarity could produce phase-dependent line ratios by altering photon pumping rates owing to eccentric orbits, or due to eclipse effects. Another possibility are corotating interaction regions (CIRs). In this case, the wind of a single star is asymmetric, yet can be modeled as stationary. Variations in f/i ratios could arise from an evolving perspective of a CIR with rotational phase, but are likely to be periodic. Our focus has been on sources of intrinsic variability for nonrotating, single stars. In this case we have split the drivers for producing time-dependent f/i ratios into two categories: stellar variability and wind variability. Issues of binarity and CIRs are deserving of separate studies for their impacts on f/i ratios.

Already Hole & Ignace (2012) explored the first category in terms of stellar pulsations for modifying the stellar radiation field to elicit changes in f/i ratios for time-steady winds. This contribution explores the second category, in which the stellar radiation is held fixed, but the wind structure is allowed to vary. Section 2 develops our approach based on integrating the line luminosities throughout the wind. In particular, we demonstrate that while the shell approximation is insensitive to changes in the mass-loss rate, variability in $\dot{M}$ can drive changes in f/i when integration across the wind is considered. Section 3 provides illustrative examples. We explore the extent to which measured line ratios may be biased in a way that depends on the observational exposure time. In Sect. 4, we provide summary remarks and comments on future work. An Appendix presents a discussion of effects from wind attentuation.

2. Model

2.1. Volume element source f/i ratio

Consider an idealized case of a small volume element in the stellar wind. This sector of gas has been heated to high temperature to emit X-rays. A generic He-like ion is assumed to exist and to produce a typical *fir* triplet emission line. The line emission is optically thin; however, the wind may be optically thick to the X-rays.

We introduce the following parameters to describe the line emission:

- L_f is the total line luminosity in the forbidden component of the triplet ($^3\mathrm{S}_1 \rightarrow {}^1\mathrm{S}_0$ transition).
- L_i is the total line luminosity in the intercombination component of the triplet ($^3\mathrm{P}_{0,1,2} \rightarrow {}^1\mathrm{S}_0$ transition).
- n_c is the critical number density of electrons for collisional excitation of electrons into the intercombination levels out of the forbidden level ($^3\mathrm{S}_1 \rightarrow {}^3\mathrm{P}_{0,1,2}$ transition).
- ϕ_c is the critical UV photon rate for radiative excitation of electrons into the intercombination levels out of the forbidden level ($^3\mathrm{S}_1 \rightarrow {}^3\mathrm{P}_{0,1,2}$ transition).
- ϕ_* is the stellar UV photon rate.
- R_0 is the ratio $L_\mathrm{f}/L_\mathrm{i}$ in the absence of any pumping processes that depopulate the forbidden level and enhance the population of the intercombination level.
- R is the ratio $L_\mathrm{f}/L_\mathrm{i}$ that allows for pumping effects.

Assuming electron densities are relatively small such that $n_\mathrm{e} \ll n_\mathrm{c}$, a well-known result for the ratio of line emission is (e.g., Kahn et al. 2001)

$$R = \frac{\mathrm{d}L_\mathrm{f}/\mathrm{d}V}{\mathrm{d}L_\mathrm{i}/\mathrm{d}V} = \frac{R_0}{1 + 2k_*\,W(r)}, \tag{1}$$

where $\mathrm{d}L_\mathrm{f}/\mathrm{d}V$ and $\mathrm{d}L_\mathrm{i}/\mathrm{d}V$ represent the luminosity contributions from the volume element, $k_* = \phi_*/\phi_\mathrm{c}$, and W is the dilution factor given by

$$W(r) = \frac{1}{2}\left[1 - \sqrt{1 - \frac{\mathcal{R}_*^2}{r^2}}\right], \tag{2}$$

for r the radius in the wind and $\mathcal{R}_*$ the stellar radius. Equation (1) for R assumes the volume element has a constant temperature. However, the ratio R_0 is weakly dependent on temperature, and so the same formula may be used in an approximate way even for a multitemperature plasma.

2.2. Shell source f/i ratio

Instead of a volume element, now consider a thin spherical shell of width $\mathrm{d}r$. Imagine the shell is traveling through the wind following a velocity profile, $v(r)$. To determine the line ratio, contributions to L_f and L_i must be accumulated for the unresolved shell, with

$$\frac{\mathrm{d}L_\mathrm{f}}{\mathrm{d}r} = 2\pi \int_{\mu_*(r)}^{+1} r^2\,\frac{\mathrm{d}L_\mathrm{f}}{\mathrm{d}V}\,\mathrm{d}\mu,$$

and

$$\frac{\mathrm{d}L_\mathrm{i}}{\mathrm{d}r} = 2\pi \int_{\mu_*(r)}^{+1} r^2 \frac{\mathrm{d}L_\mathrm{i}}{\mathrm{d}V}\, \mathrm{d}\mu,$$

where $\mu = \cos\theta$ for θ the polar angle from the observer's line of sight, $\mu_*(r) = \sqrt{1 - \mathcal{R}_*^2/r^2}$ accounts for stellar occultation of part of the shell when at radius r in the wind, and because of symmetry integration in the azimuth ϕ about the observer's axis has already been carried out.

For a thin spherical shell, the two integrals yield a result that is the same as for a small volume element, where

$$R = \frac{\mathrm{d}L_\mathrm{f}/\mathrm{d}r}{\mathrm{d}L_\mathrm{i}/\mathrm{d}r} = \frac{R_0}{1 + 2k_*\, W(r)}. \tag{3}$$

Given that R_0 is a constant, the only way to produce variability in the ratio R is either for k_* to change, or for the location of the shell, r, to change. Hole & Ignace (2012) explored the possibility of a time-dependent R being driven by variability in the stellar radiation field. In this work, the focus is on factors that alter R owing to wind structure.

For a simple spherical shell, ignoring the temperature influence, i.e., assuming R_0 is fixed and that the hot plasma has a temperature adequate to produce the line emission under consideration, variations in R naturally arise as the shell evolves through the wind. For illustrative purposes, consider a shell that is coasting at constant speed with $v(r) = v_0$. After a time-of-flight t, with the shell originating at the stellar surface, the radial location of the shell becomes

$$r(t) = \mathcal{R}_* + v_0\, t. \tag{4}$$

Time-dependence in the line ratio R enters through the dilution factor. The dilution factor ranges from 0.5 (at $r = \mathcal{R}_*$) to 0.0 (as $r \to \infty$), hence $2W$ ranges between 0 and 1. At large distance, $W \propto r^{-2}$. If $k_* \gg 1$, the shell may have to travel great distance before R changes.

As a more realistic case, the velocity profile of a stellar wind is frequently approximated as a beta-law and is written as

$$v(r) = v_\infty\, (1 - bu)^\beta, \tag{5}$$

where $u = \mathcal{R}_*/r$ is a normalized inverse radius, and b is a constant that serves to set the initial wind speed at the wind base, where $v_0 = v_\infty\,(1-b)$. For use as an example, we introduce a normalized velocity with $\beta = 1$ as follows:

$$w(u) = v/v_\infty = 1 - bu. \tag{6}$$

Figure 1 illustrates the characteristic time over which R varies as a geometrically thin shell moves through the wind following the velocity law, $w(u)$. We note that at large distance, $R \to R_0$, and the line ratio has a minimum of $R_\mathrm{min} = 1/(1 + k_*)$ when the shell is at $r = \mathcal{R}_*$. We define $t_{1/2}$ as the time of flight for the shell until $R = 0.5(R_\mathrm{min} + R_0)$.

The upper panel of Fig. 1 gives $t_{1/2}/t_\infty$, where $t_\infty = \mathcal{R}_*/v_\infty$ is the characteristic flow time for the wind, against k_* in a log–log plot. Vertical lines are for different He-like ion species assuming a stellar radiation field for ζ Pup, using a Kurucz model with $T_\mathrm{eff} = 40,100$ K and $\log g = 3.65$ (Cassinelli et al. 2001). For a different star, the vertical lines would shift laterally for the appropriate radiation field at the stellar surface. We note that for massive star winds, t_∞ is of order hours or a day. What the upper panel shows is that different lines tend to have different response

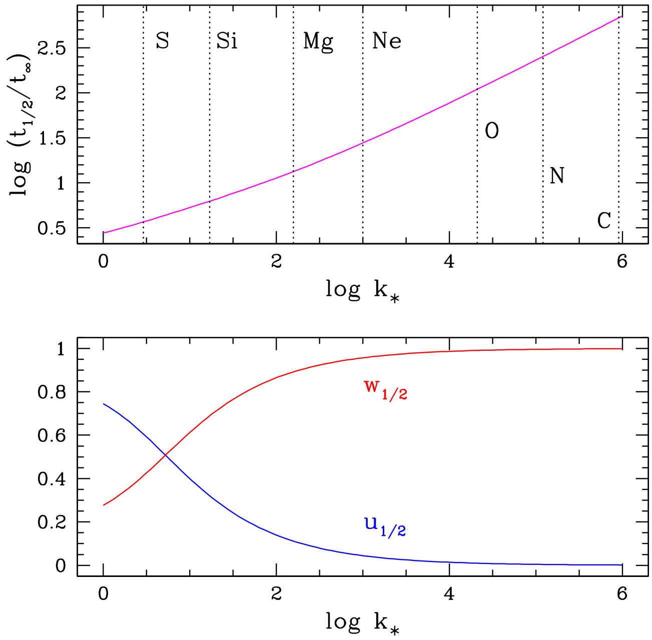

Fig. 1. For an X-ray emitting shell moving through a wind with a $\beta = 1$ velocity law, characteristic time, distance, and velocity for which the $R = f/i$ line ratio changes. *Upper panel*: characteristic time $t_{1/2}$, relative to the wind flow time, t_∞. *Lower panel*: distance and velocity in the wind corresponding to $t_{1/2}$. See text for explanation of the vertical lines in the upper panel.

times for how R varies. The lower panel shows where in inverse radius, $u_{1/2}$, or in normalized velocity, $w_{1/2}$, the ratio $t_{1/2}/t_\infty$ is achieved as a function of k_*.

Before exploring the line ratio based on integration throughout the wind, it is worth noting that for a shell at a fixed location, the line ratio is insensitive to a time variable wind density. While the emission in all of the triplets changes with density, they all rise or fall by the same factor for X-ray emission produced at a fixed distance from the star.

2.3. Distributed sources f/i ratio

Leutenegger et al. (2006) presented an approach for evaluating the emission line ratio when the hot plasma is distributed throughout the wind. Assuming spherical symmetry and optically thin line emission, the emissivities for the forbidden and intercombination components are given by

$$j_\mathrm{f} \propto \frac{\tilde{R}}{1 + \tilde{R}}\, \rho^2 \tag{7}$$

and

$$j_\mathrm{i} \propto \frac{1}{1 + \tilde{R}}\, \rho^2, \tag{8}$$

where $\rho(r)$ is the mass density of the hot plasma in the wind, and

$$\tilde{R}(r) = \frac{\mathrm{d}L_\mathrm{f}/\mathrm{d}r}{\mathrm{d}L_\mathrm{i}/\mathrm{d}r} = \frac{R_0}{1 + 2k_*\, W(r)}. \tag{9}$$

Since R is the notation for the observed line ratio, the addition of a tilde in the above merely signifies the ratio for just one shell in the wind in which hot plasma is distributed over a range of radii. The luminosities in the respective lines are given by

$$L_{\rm f,i} \propto \int j_{\rm f,i}\,(1-W)\,r^2\,{\rm d}r, \tag{10}$$

where the parenthetical involving the dilution factor accounts for the effect of stellar occultation.

It is possible to recast the line ratio to mimic somewhat the classic result for a shell in Eq. (3). Using inverse radius $u = \mathcal{R}_*/r$, we begin as follows:

$$\frac{1}{1+\tilde{R}} = \frac{1+2k_*\,W}{A_0 - k_*\,\sqrt{1-u^2}}, \tag{11}$$

where

$$A_0 = 1 + R_0 + k_*. \tag{12}$$

Then

$$\frac{\tilde{R}}{1+\tilde{R}} = \frac{R_0}{A_0 - k_*\,\sqrt{1-u^2}}. \tag{13}$$

With these conversions, using the normalized wind velocity $w = v/v_\infty$, and inserting $\rho \propto u^2/w$, the luminosity for forbidden line emission is

$$L_{\rm f} = L_0\,R_0 \int \left[\frac{1}{A_0 - k_*\,\sqrt{1-u^2}}\right](1-W)\,\frac{{\rm d}u}{w^2} \equiv L_0\,R_0\,\Lambda_0, \tag{14}$$

where L_0 is a constant that cancels when taking the line ratio. Next,

$$\begin{aligned} L_{\rm i} &= L_0\,R_0 \int \left[\frac{1+2k_*\,W}{A_0 - k_*\,\sqrt{1-u^2}}\right](1-W)\,\frac{{\rm d}u}{w^2} \\ &= L_0 \left\{\frac{L_{\rm f}}{R_0}(1+k_*) - k_* \int \left[\frac{\sqrt{1-u^2}}{A_0 - k_*\sqrt{1-u^2}}\right](1-W)\,\frac{{\rm d}u}{w^2}\right\} \\ &\equiv L_0\,\Lambda_0\,(1+k_*) - L_0\,k_*\,\Lambda_1. \end{aligned} \tag{15}$$

We note that in all of the preceding integrals, the upper and lower limits are formally for the radial intervals over which the line in question forms. In principle, there could be multiple such radial zones, and their locations and spatial extents could be functions of time.

The line ratio, now involving all of the forbidden and intercombination line emission separately evaluated throughout the wind, becomes

$$\frac{L_{\rm f}}{L_{\rm i}} = R = \frac{R_0\Lambda_0}{(1+k_*)\,\Lambda_0 - k_*\,\Lambda_1}. \tag{16}$$

Finally, we can recast this relation as

$$R \equiv \frac{R_0}{1 + k_*\,(1-\xi)}, \tag{17}$$

where $\xi = \Lambda_1/\Lambda_0$, and the overall expression bears strong similarity to Eq. (1) with $1-\xi$ acting in the place of $2W(r)$. For $r \to \infty$, $\xi \to 1$. The minimum value of ξ for $r = \mathcal{R}_*$ depends on line-specific parameters, but can be as low as zero. All of the effects of wind integration are collected in the parameter ξ. This parameter also depends on factors that are specific to the line under consideration, where $\xi = \xi(R_0, k_*, u_{\rm min}, u_{\rm max})$, and $u_{\rm min}$ and $u_{\rm max}$ are limits for the wind integration that are set by where X-ray production occurs, or by specifics of the temperature distribution relevant to the line in question. As a result, ξ differs from one triplet to the next.

The expressions above for wind integration can also take into account photoabsorption of X-rays by the wind. The inclusion of this effect does not alter the key result of Eq. (17). Photoabsorption introduces an exponential factor of wind optical depth in the respective integrands for the forbidden and intercombination line emissions. With wind absorption the two line luminosity expressions become

$$L_{\rm f} = L_0'\,R_0 \int\!\!\int \left[\frac{1}{A_0 - k_*\,\sqrt{1-u^2}}\right](1-W)\,{\rm e}^{-\tau(u,\mu)}\,\frac{{\rm d}u}{w^2}\,{\rm d}\mu, \tag{18}$$

and

$$L_{\rm i} = L_0'\,R_0 \int\!\!\int \left[\frac{1+2k_*\,W}{A_0 - k_*\,\sqrt{1-u^2}}\right](1-W)\,{\rm e}^{-\tau(u,\mu)}\,\frac{{\rm d}u}{w^2}\,{\rm d}\mu, \tag{19}$$

where the wind optical depth is

$$\tau(u,\mu) = \int \kappa\,\rho\,{\rm d}z. \tag{20}$$

The coefficient changes with $L_0 \to L_0'$ because the integration is now a double integral in both inverse radius u as well as polar angle in the form of μ, since the optical depth is evaluated along a ray of fixed impact parameter. Many authors have presented ways of handling wind absorption (e.g., Leutenegger et al. 2010). The appendix provides further discussion on the topic. In what follows the wind absorption is ignored for the sake of example cases.

3. Model results

Wind integration enlarges the possibilities for variability not just in the separate emission lines of the triplet, but in the ratio R as well. Focusing strictly on drivers of variability from changes in the wind (i.e., ignoring changes in k_*), factors that could induce variability in R include changes in the wind density and changes in the temperature distribution. For the wind density, global changes to the wind might include the mass-loss rate $\dot{M}$, or the wind velocity law. Time dependence in any of $\dot{M}$, v_∞, b, or β would lead to time dependence in ρ. This is a particularly interesting result, since a shell model has no sensitivity to density variations. Time dependence of the temperature distribution for the hot plasma influences R as well. This can arise from changes in the range of temperatures achieved in the wind or the radial profile of the distribution.

However, whether in the density or in the temperature distribution, creating an observable $R(t)$ mainly results if there is a global change in the wind, as opposed to distributed and stochastic changes that effectively produce a steady-state wind.

As an illustrative case, we consider a sinusoidal variation in the mass-loss rate. This variation is modeled with

$$\dot{M}(t) = \dot{M}_0 + \delta\dot{M}\,\sin(\omega t - \Phi_0), \tag{21}$$

where $\dot{M}_0$ is the average value of the mass-loss rate, $\delta\dot{M}$ is an amplitude for the variation, $\omega = 2\pi/P$ is the angular frequency for period P associated with the cyclical variation, and Φ_0 is an arbitrary phase. We note that $\delta\dot{M} \le \dot{M}_0$, otherwise density would become negative.

However, Eq. (21) is how the mass loss varies at the base of the wind. The density perturbation elsewhere depends on the flow time between the base and the radius of interest. To determine the density at all radii in the wind, we must determine the time lag between the radius r and the surface $\mathcal{R}_*$. This time lag, $t_{\rm lag}$, is the time of travel through the wind. For the sake of illustration, we assume the velocity is a $\beta = 1$ velocity law. The time lag then becomes

$$t_{\rm lag} = t_\infty \left\{ \frac{1-u}{u} + b \, \ln\left[\frac{1-bu}{(1-b)\,u}\right]\right\} \equiv t_\infty \, \gamma(u), \tag{22}$$

where again $t_\infty = \mathcal{R}_*/v_\infty$ is the characteristic flow time in the wind. Now the mass-loss rate at any location in the wind at any time is

$$\dot{M}(u,t) = \dot{M}_0 + \delta\dot{M} \, \sin\left\{2\pi \left[\frac{t}{P} - \frac{t_\infty}{P}\,\gamma(u)\right] - \Phi_0\right\}. \tag{23}$$

The density is given by

$$\rho(t,u) \propto \frac{\dot{M}(t,u)}{w(u)}\, u^2. \tag{24}$$

The formulations for Λ_0 and Λ_1 are unchanged, except they now become functions of time following the integration over volume, because the density undulates as a propagating wave.

The result for the line ratio is

$$R(t) = \frac{R_0}{1 + k_*\,[1-\xi(t)]}. \tag{25}$$

Examples of $R(t)$ plotted with phase for cyclic variability in the mass loss are shown in Fig. 2, with two cycles shown for better display of the variation. The different curves are for different values of $\delta\dot{M}/\dot{M}_0$. The upper panel shows the relative luminosity in the forbidden line. The middle section shows the intercombination line. The lower panel indicates the line ratio relative to R_0. In this lower panel, the horizontal line in magenta is the result when mass loss is constant (i.e., $\delta\dot{M} = 0$). The vertical green lines indicate the minimum and maximum in R for $\delta\dot{M}/\dot{M}_0 = 0.9$, as a specific example allowing comparison between the extrema in the line ratio with the individual line luminosities. All of the curves represent $\Phi_0 = 0$.

For this figure we adopt parameters similar to ζ Pup as a general guideline. We also used a ratio of $t_\infty/P = 0.1$. The value of ξ depends on the choice of R_0; a value of $R_0 = 2.5$ for Si XIII was used for this example (Blumenthal et al. 1972). We again adopt the stellar radiation field used by Cassinelli et al. (2001) for ζ Pup, which gives $k_* = 16.9$ for the rate of UV pumping of the f-line component at the stellar surface. For the volume integration of line luminosities, the X-rays are considered to exist from the stellar surface ($u_{\rm max} = 1$) to infinity ($u_{\rm min} = 0$).

There are several features worth noting about Fig. 2. To begin, the peaks are much taller than the troughs are deep. The emissivity scales with the square of density. As a result, a snapshot of the wind reveals alternating over- and under-density zones relative to the mean. With a ρ^2 emissivity, the series of shells act much like a clumped wind. But since the UV pumping is strongest at the inner wind, the presence of an increased density at locations where the UV pumping is diminished can considerably enhance the luminosity in the forbidden line, relative to a time-steady flow. The intercombination line is enhanced where pumping is strong, so the demoninator for the line ratio is also changing. The vertical green lines are guides to aid in comparing the state of the respective line luminosities to the varying line ratio.

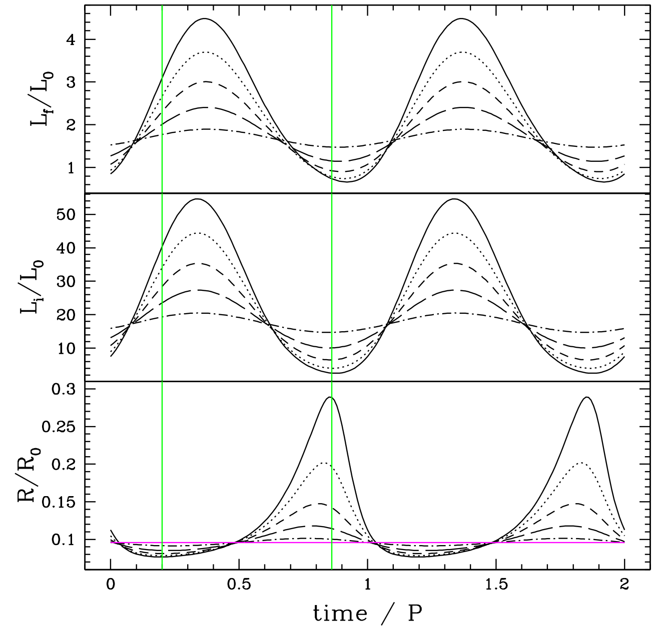

Fig. 2. Variability in the forbidden line luminosity (*upper*), intercombination line luminosity (*middle*), and the line ratio (*lower*). Here, L_0 is a constant, and R_0 is the line ratio in the absence of UV pumping. These are plotted against time relative to the period P for variability in the mass-loss rate. The different curves indicate $\delta\dot{M}/\dot{M}_0 =$ 0.1 (dash-dot), 0.3 (long dash), 0.5 (short dash), 0.7 (dotted), and 0.9 (solid). In the lower panel, the horizontal line in magenta indicates $\delta\dot{M} = 0.0$. The two vertical green lines represent the minimum and maximum values of R/R_0 when $\delta\dot{M}/\dot{M}_0 = 0.9$. Two cycles of the periodic variability are shown for clarity of viewing.

In Fig. 2 the emission is assumed to form from the wind base at $\mathcal{R}_*$ to infinite distance, although emission at a very large radius has minimal contribution to the line flux. However, many studies treat the inner radius for the production of X-rays as a free parameter for model fits. For example, in a line profile analysis of several lines measured by *Chandra* for ζ Pup, Cohen et al. (2010) found that X-rays were produced from $r_0 = 1.5\mathcal{R}_*$ and beyond. Figure 3 compares examples with values of $r_0/\mathcal{R}_* = 1.0$ (long dash), 1.1 (short dash), 1.5 (dotted), and 2.0 (solid), which all have $\delta\dot{M}/\dot{M}_0 = 0.3$. The cases have different values for R in the absence of variable mass-loss; consequently, Fig. 3 shows a relative variation for ease of comparison, where each case is normalized to $\bar{R}(r_0)$ as the value for its nonvarying wind. The shapes are generally similar, although phase shifted owing to time lags for the flow traversing the gap $r_0 - \mathcal{R}_*$. The relative peak-to-trough amplitudes are actually nonmonotonic with r_0, but ultimately drops as r_0 increases to larger values, as the radiative pumping becomes weaker with distance.

Another consideration is to vary the ratio t_∞/P, with a selection of examples shown in Fig. 4. As in Fig. 3, $\delta\dot{M}/\dot{M}_0 = 0.3$ is held fixed. The three panels follow those of Fig. 2, now with $t_\infty/P = 0.03$ (solid), 0.1 (dotted), 0.3 (long dash), 1.0 (short dash), and 3.0 (dash-dot). Altering the period at which $\dot{M}$ is varied relative to the wind flow time leads to both phase shifting in the pattern and amplitude changes. The amplitude of variation in R drops as t_∞/P increases. For a wind with relatively high frequency oscillations in $\dot{M}$, the wind density varies over short length scales, and the wind integrations for L_f and L_i obtain values for the time-averaged stationary wind.

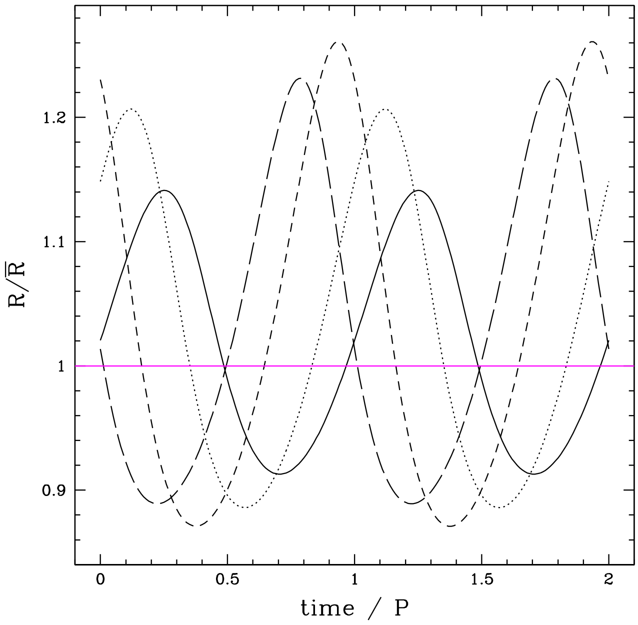

Fig. 3. Comparison of $R = f/i$ line ratios when the line forms beyond radius r_0. The quantity $r_0/\mathcal{R}_* = 1.0$ (long dash), 1.1 (short dash), 1.5 (dotted), and 2.0 (solid), where $\delta\dot{M}/\dot{M}_0 = 0.3$. The quantity R is normalized to $\bar{R}$, which is the value for the line ratio when $\delta\dot{M} = 0$ for the respective cases. Thus, the curves represent relative changes to a nonvarying wind, indicated as the horizontal line in magenta.

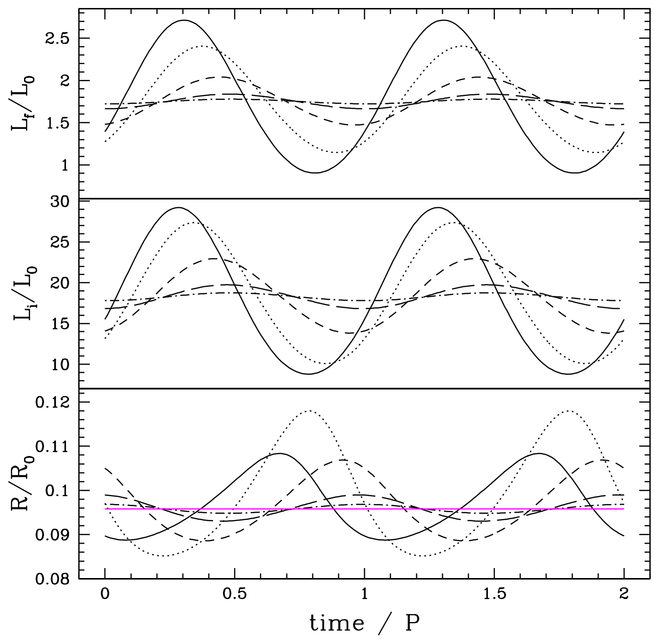

Fig. 4. Similar to Fig. 2 but with $\delta\dot{M}/\dot{M}_0 = 0.3$ and different ratios of $t_\infty/P = 0.03$ (solid), 0.1 (dotted), 0.3 (short dash), 1.0 (long dash), and 3.0 (dash-dot).

Returning to Fig. 2, perhaps the most important point is that these curves portray a snapshot of the wind, as if measures for L_f and L_i were instantaneous. However, single massive stars are relatively faint X-ray sources. The exposures required to obtain sufficient counts for high signal-to-noise line fluxes with current facilities are measured in many kiloseconds of data collection.

In practice we are not concerned so much about the variable luminosity of the forbidden and intercombination lines so much as the accumulated counts (or energy) over the course of an exposure. Figure 5 shows how exposure time affects the measured value of the line ratio that includes the time-varying wind density. The two upper panels plot the cumulative counts in the i and f lines, respectively, against the exposure time as normalized to the period for the variation in mass loss. The relative scale is arbitrary, since what matters for R is the ratio of the two line luminosities.

If the X-ray luminosities in the lines were constant, the counts would grow linearly in time. However, the variability in the mass-loss rate imposes the wavy structure seen on the otherwise linear growth in both the i and f line counts. The different colors indicate eight different phases, with $\Phi_0 = 0°, 45°, 90°, 135°, 180°, 225°, 270°$, and 315°.

The lower panel shows the line ratio as a function of the exposure time for the observation, again in terms of the period of variability for $\dot{M}$. The curves represent $\delta M/\dot{M}_0 = 0.3$. Figure 5 shows that if the period is long compared to the exposure, then the line counts and the resulting line ratio R basically reflect a snapshot for the current state of the wind's inner density. However, if the exposure time is relatively long, then the oscillatory perturbation in the wind becomes diminishingly relevant in terms of the accumulated counts. As a result, the line ratio R achieves a value for the wind as if it were nonvarying, at the time-averaged mass-loss rate $\dot{M}_0$. Since the emissivity scales as ρ^2, a roughly t^{-2} decline in the variation of R relative to a nonvarying wind results; overplotted is an envelope for a decline in amplitude with t^{-2} shown a dotted lines.

It is useful to explore observational prospects for detecting effects shown in Fig. 5. Since parameters for ζ Pup were adopted in the examples, existing data for this star are considered. While considerable data have been obtained with the *XMM-Newton* (e.g., Nazé et al. 2018), the various datasets are spread over many years and not suitable for this type of study. Cassinelli et al. (2001) obtained 67 ks of continuous high-resolution *Chandra* data for ζ Pup. This corresponds to an exposure of about 19 h. Using radius and terminal speed values from that paper, the flow time is $t_\infty = 1.6$ h, and the *Chandra* exposure is nearly 12 flow times; this is not far from the value of 10 flow times used in our examples. Cassinelli et al. (2001) measured $R = 1.04 \pm 0.14$ for SiXIII, which is a 13% uncertainty in R/R_0. Figure 5 suggests that R/R_0 might be 5% higher or lower than the long-term value. One would need multiple pointings of a similar duration at an accuracy of around 1% to detect the envelope of variability, assuming $\delta\dot{M}/\dot{M} = 0.3$. This would allow the creation of a scatter plot of values from the multiple pointings, which could be compared with a diagnostic plot like Fig. 5. Assuming variability is not regular in the long term (e.g., repeating with phase), the ensemble of measures should fill in the envelope of possibilities, namely between the t^{-2} pair of curves. Existing data do not appear adequate to the purpose. Of course, larger values of $\delta\dot{M}/\dot{M}$ would be easier to detect, while smaller variations would be harder.

4. Conclusion

In this paper we have explored drivers of variable $R = f/i$ line luminosity ratios for the wind from UV-bright massive stars, with application to variable mass loss as a quantitative example. Whereas a previous paper described the influence of a variable stellar radiation field (Hole & Ignace 2012), in this work the focus has been on variability within the wind itself. This variability can arise from altering anything that can change the emissivity of line production (e.g., temperature structure

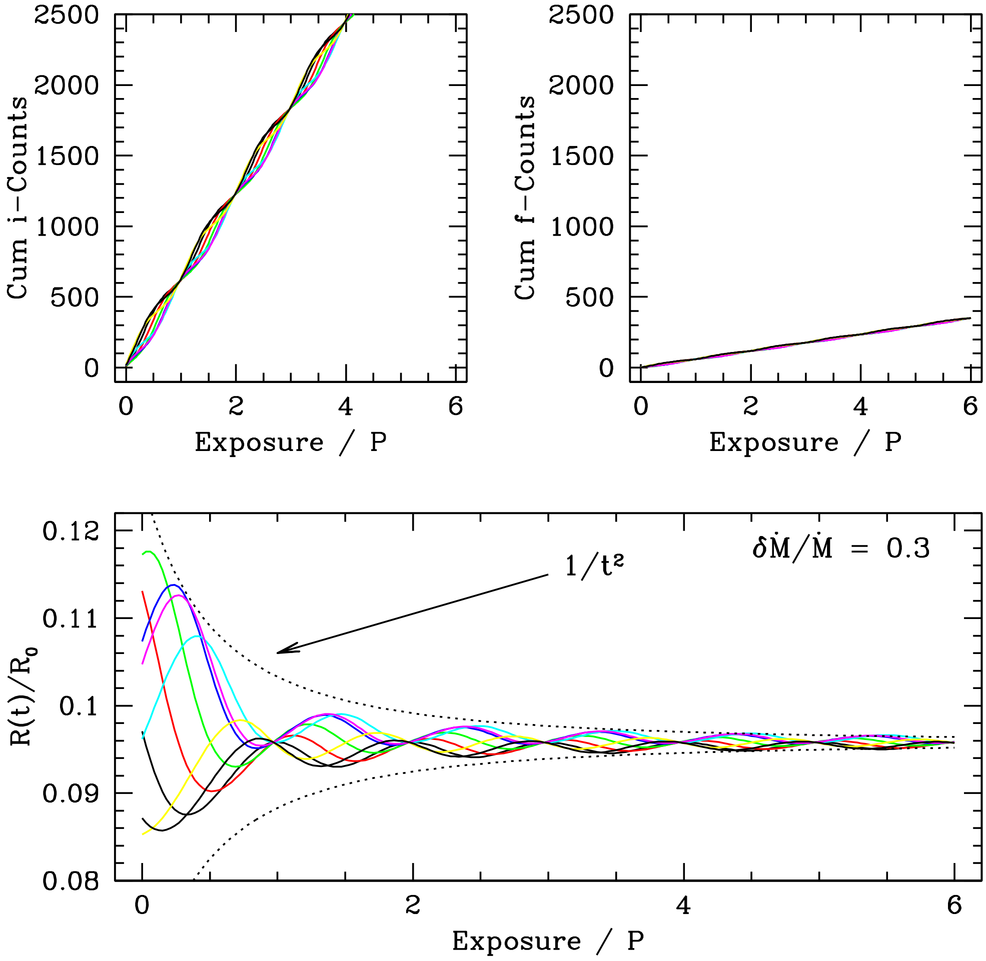

Fig. 5. Effect of exposure time for a hypothetical observation of a He-like triplet. *Upper left*: cumulative counts in the i-component of the triplet with exposure time, as normalized to the period for variability in the mass-loss rate. *Upper right*: cumulative counts in the f-component. *Bottom*: line ratio. The different curves show different phase values, Φ_0 (see text). The example depicts $\delta\dot{M}/\dot{M}_0 = 0.3$ for Si XIII with stellar parameters for ζ Pup. Also shown in the lower panel in dotted line type is a t^{-2} decay envelope.

or density structure). However, in order to achieve significant variations in R, the variation in the wind must be global in nature. Small-scale stochastic variations do not much engender time-dependence in the line ratio R.

As proof of concept, we considered a variable mass-loss rate, taken simply as a sinusoid in time with period P. The X-ray emissivity for line cooling is density squared, and so the smoothly undulating density with radius affects the line emission much as clumping in the form of spherical shells. This affects both the forbidden and intercombination lines equally in terms of density; however, the UV pumping of the forbidden line population serves as an additional radius-dependent weighting factor for determination of the respective line luminosities. As a result, a periodic, but nonsinusoidal, variation in R persists.

Observations are obtained over relatively long exposure times. Allowing for the accumulation of line counts over time shows that the relevance of variable f/i ratios depends on how the exposure time for the observations compare to the period of the variable mass loss. If the exposure time is short compared to P, then the f/i ratio may be biased in terms of the phase of $\dot{M}(t)$ at which data were obtained. An analysis based on a steady-wind model would thus lead to errors in the distribution of the hot plasma, in relation to the stellar atmosphere. If the exposure is long, the effects of time-varying wind density averages out in the accumulation of line counts, and the measured value of R obtains a value representing the time-averaged spherical wind.

In practice, long observation times are not generally achieved in a single continuous exposure. Instead, a source may be visited multiple times, each one a subexposure for the program. These subexposures may not be of equal duration nor equally spaced in time. They are likely obtained over the span of a year since most programs run on an annual cycle. While we did not conduct simulations for ensembles of subexposures, the logic above still applies. If the duty cycle of the subexposures is long compared to P, then the wind is effectively randomly sampled. But if P is long, then the various subexposures essentially sample a relatively fixed phase for the wind. Understanding how observed f/i ratios may be biased for the in-between cases would require further model simulations.

We note that Dyda & Proga (2018) have presented results for 1D time-dependent hydrodynamical simulations for line-driven winds with a sinusoidally varying stellar radiation field on a period T_S ("S" for source). We can associate our period, P, for the varying $\dot{M}$ with their period notation. They have then introduced a dynamical time as a ratio of the radius for the wind critical point, r_c, to the flow speed at the critical point, v_c. Supposing $r_c = \mathcal{R}_*$, and $v_c = v_0$, the latter being the wind speed at the base of the wind, then in terms of our flow time, their dynamical time becomes $t_c = (v_\infty/v_0)\, t_\infty \sim 10^2\, t_\infty$. Dyda & Proga (2018) have found that for $P \gg t_c$, the wind oscillates between so-called high and low states, meaning the wind mass loss reflects the state of the stellar radiation field. When $P \ll t_c$, the wind is largely stationary as if driven by a constant radiation flux (i.e., the average radiation field of the star). All of our examples in this paper are in the long-period regime of Dyda & Proga (2018), since even $t_\infty/P = 3$ (see Fig. 4) corresponds only to $t_c/P \sim 0.03$.

While Hole & Ignace (2012) considered the effects of a variable radiation field for producing variability in f/i line ratios and this paper has emphasized the effects of variable wind structure, the two may well be linked. The examples in this paper were limited to fluctuating mass loss. To explore how f/i ratios could be impacted when both $\dot{M}$ and the stellar luminosity L_* are time-dependent, we consider a line-driven wind: Lamers & Cassinelli (1999) stated that $\dot{M} \sim L_*^{1.5}$, which implies $\delta\dot{M}/\dot{M} \sim 1.5\,\delta L_*/L_*$. Assume that the stellar luminosity variations occur for a star of fixed radius, then $\delta L_*/L_* = 4\delta T_*/T_*$. In the hottest star considered by Hole & Ignace (2012; $T_* = 40\,000$ K, similar to that of ζ Pup and the examples of this paper), the wavelength for pumping associated with Si XIII is approximately in the Rayleigh-Jeans tail of the blackbody, and thus linear in T_*, implying that $k_* \propto T_*$ for this scenario. This relation also implies that the variable mass loss and luminosity are in phase. With $\delta T_*/T_* = (1/6)\delta\dot{M}/\dot{M}$, and $\delta\dot{M}/\dot{M} = 0.3$, we found that the range of variation of R/R_0 in Fig. 2 increased by less than 5%, thus the response to phased luminosity changes is less than linear. However, this example artificially fixes the stellar radius, does not take account of non-radial pulsations, and considers only the Rayleigh-Jeans limit. The extent to which different lines respond to both wind structure and variable luminosity will be an interesting study for a future paper.

Acknowledgements. We are grateful to an anonymous referee for comments that have improved this manuscript. We thank Wayne Waldron for his support and insights concerning the topic of this study. This research was supported by NASA grant G08-19011F for the *Chandra* General Observer Program, Cycle 19.

References

Aerts, C., & Rogers, T. M. 2015, ApJ, 806, L33
Baum, E., Hamann, W.-R., Koesterke, L., & Wessolowski, U. 1992, A&A, 266, 402
Berghoefer, T. W., Schmitt, J. H. M. M., Danner, R., & Cassinelli, J. P. 1997, A&A, 322, 167
Blomme, R., van de Steene, G. C., Prinja, R. K., Runacres, M. C., & Clark, J. S. 2003, A&A, 408, 715
Blumenthal, G. R., Drake, G. W. F., & Tucker, W. H. 1972, ApJ, 172, 205
Cantiello, M., Langer, N., Brott, I., et al. 2009, A&A, 499, 279
Cassinelli, J. P., Waldron, W. L., Sanders, W. T., et al. 1981, ApJ, 250, 677
Cassinelli, J. P., Miller, N. A., Waldron, W. L., MacFarlane, J. J., & Cohen, D. H. 2001, ApJ, 554, L55
Castor, J. I., Abbott, D. C., & Klein, R. I. 1975, ApJ, 195, 157
Cohen, D. H., Leutenegger, M. A., Wollman, E. E., et al. 2010, MNRAS, 405, 2391
Cohen, D. H., Wollman, E. E., Leutenegger, M. A., et al. 2014, MNRAS, 439, 908
Dyda, S., & Proga, D. 2018, MNRAS, 481, 5263
Eversberg, T., Lépine, S., & Moffat, A. F. J. 1998, ApJ, 494, 799
Feldmeier, A., Puls, J., & Pauldrach, A. W. A. 1997, A&A, 322, 878
Feldmeier, A., Oskinova, L., & Hamann, W.-R. 2003, A&A, 403, 217
Friend, D. B., & Abbott, D. C. 1986, ApJ, 311, 701
Fullerton, A. W., Massa, D. L., & Prinja, R. K. 2006, ApJ, 637, 1025
Gabriel, A. H., & Jordan, C. 1969, MNRAS, 145, 241
Gayley, K. G. 1995, ApJ, 454, 410
Gayley, K. G., Owocki, S. P., & Cranmer, S. R. 1995, ApJ, 442, 296
Güdel, M., & Nazé, Y. 2009, A&ARv, 17, 309
Harnden, Jr., F. R., Branduardi, G., Elvis, M., et al. 1979, ApJ, 234, L51
Hillier, D. J. 1991, A&A, 247, 455
Hole, K. T., & Ignace, R. 2012, A&A, 542, A71
Huenemoerder, D. P., Gayley, K. G., Hamann, W. R., et al. 2015, ApJ, 815, 29
Ignace, R. 2001, ApJ, 549, L119
Ignace, R. 2016, Adv. Space Res., 58, 694
Ignace, R., & Gayley, K. G. 2002, ApJ, 568, 954
Ignace, R., & Oskinova, L. M. 1999, A&A, 348, L45
Ignace, R., Oskinova, L. M., & Foullon, C. 2000, MNRAS, 318, 214
Kahn, S. M., Leutenegger, M. A., Cottam, J., et al. 2001, A&A, 365, L312
Krtička, J., & Kubát, J. 2016, Adv. Space Res., 58, 710
Lamers, H. J. G. L. M., & Cassinelli, J. P. 1999, Introduction to Stellar Winds (Cambridge: Cambridge University Press), 452
Langer, N. 2012, ARA&A, 50, 107
Leutenegger, M. A., Paerels, F. B. S., Kahn, S. M., & Cohen, D. H. 2006, ApJ, 650, 1096
Leutenegger, M. A., Cohen, D. H., Zsargó, J., et al. 2010, ApJ, 719, 1767
Leutenegger, M. A., Cohen, D. H., Sundqvist, J. O., & Owocki, S. P. 2013, ApJ, 770, 80
Lucy, L. B. 1983, ApJ, 274, 372
Lucy, L. B., & Abbott, D. C. 1993, ApJ, 405, 738
Lucy, L. B., & Solomon, P. M. 1970, ApJ, 159, 879
Lucy, L. B., & White, R. L. 1980, ApJ, 241, 300
Nazé, Y. 2009, A&A, 506, 1055
Nazé, Y., Ramiaramanantsoa, T., Stevens, I. R., Howarth, I. D., & Moffat, A. F. J. 2018, A&A, 609, A81
Oskinova, L. M., Feldmeier, A., & Hamann, W.-R. 2006, MNRAS, 372, 313
Oskinova, L. M., Hamann, W.-R., & Feldmeier, A. 2007, A&A, 476, 1331
Oskinova, L. M., Huenemoerder, D. P., Hamann, W.-R., et al. 2017, ApJ, 845, 39
Owocki, S. P., & Cohen, D. H. 1999, ApJ, 520, 833
Owocki, S. P., & Cohen, D. H. 2001, ApJ, 559, 1108
Owocki, S. P., & Cohen, D. H. 2006, ApJ, 648, 565
Owocki, S. P., Castor, J. I., & Rybicki, G. B. 1988, ApJ, 335, 914
Pauldrach, A., Puls, J., & Kudritzki, R. P. 1986, A&A, 164, 86
Porquet, D., Mewe, R., Dubau, J., Raassen, A. J. J., & Kaastra, J. S. 2001, A&A, 376, 1113
Postnov, K. A., & Yungelson, L. R. 2014, Liv. Rev. Rel., 17, 3
Prinja, R. K., Barlow, M. J., & Howarth, I. D. 1990, ApJ, 361, 607
Puls, J., Markova, N., Scuderi, S., et al. 2006, A&A, 454, 625
Puls, J., Vink, J. S., & Najarro, F. 2008, A&ARv, 16, 209
Robert, C. 1992, Ph.D. Thesis, Université de Montreal, Canada
Sana, H., de Mink, S. E., de Koter, A., et al. 2012, Science, 337, 444
Skinner, S., Güdel, M., Schmutz, W., & Zhekov, S. 2006, Ap&SS, 304, 97
Smith, N. 2014, ARA&A, 52, 487
Springmann, U. 1994, A&A, 289, 505
Vanbeveren, D., De Loore, C., & Van Rensbergen, W. 1998, A&ARv, 9, 63
Waldron, W. L., & Cassinelli, J. P. 2001, ApJ, 548, L45
Waldron, W. L., & Cassinelli, J. P. 2007, ApJ, 668, 456
Waldron, W. L., & Cassinelli, J. P. 2010, ApJ, 711, L30

Appendix A: Effects of wind attenuation on the *f/i* line ratio

Some winds are sufficiently dense that photoabsorptive opacity suppresses the escape of X-rays from the wind and influences the ionization balance in the wind (e.g., Baum et al. 1992; Waldron & Cassinelli 2010; Krtička & Kubát 2016). The effect can depend on abundances, owing to the large cross sections of metal ions (e.g., solar versus metal-rich such as Wolf-Rayet stars; see Ignace & Oskinova 1999). The cross section scales roughly as cube of the wavelength, λ^3, so the strength of photoabsorption ranges substantially across an X-ray spectrum, from being significant at soft energies to potentially irrelevant at high energies. Since radiative pumping is strongest for X-rays formed closest to the star, and since photoabsorption (when relevant) absorbs the innermost X-rays of the wind, attenuation effects can impact the observed f/i line ratios (e.g., the observed f/i line ratios for WR 6, with a dense wind, are consistent with no UV pumping; Huenemoerder et al. 2015). In terms of variability, attenuation modifies where in the wind X-rays can escape to the observer, and as indicated in the discussion for Figs. 1 and 3, location determines the timescale and amplitude of variability in f/i ratios.

The inclusion of photoabsorption to determine emergent line luminosities throughout the wind is straightforward, with

$$L_{\mathrm{f,i}} = \int_{\mathcal{R}_*}^{\infty} \int_{\mu_0(r)}^{+1} 2\pi\, j_{\mathrm{f,i}}\, \mathrm{e}^{-\tau(r,\mu)}\, r^2\, \mathrm{d}r\, \mathrm{d}\mu, \tag{A.1}$$

where $\mu_0(r)$ accounts for the effect of stellar occultation, and the optical depth to photoabsorption is

$$\tau(r,\mu,\lambda) = \int \kappa(\lambda)\, \rho(r)\, \mathrm{d}z. \tag{A.2}$$

The opacity $\kappa(\lambda)$ does not vary much between triplet components of a given He-like species, but can change significantly from the triplets of one species to the next. The density ρ refers to the "cool" component (not X-ray producing), which produces features such as UV P Cygni lines. The optical depth is for a ray of fixed impact parameter, hence the integration in z.

Without photoabsorption, the line luminosity calculation is a 1D integral in radius; with it, the evaluation is a 2D integral. However, a 1D integral can be recovered using the exospheric approximation (example applications of the exospheric approximation for stellar wind X-rays include Owocki & Cohen 1999; Ignace et al. 2000). The exospheric approximation does not produce quantitatively accurate results; however, it can produce qualitatively accurate trends, and therefore we employ it for heuristic purposes.

The approximation is to determine the radius along the line of sight to the star, where $\tau(E) = 1$, denoted as $r_1(E)$. This radius is treated as a hard spherical boundary for which no X-rays escape when $r < r_1$, and X-rays formed at $r > r_1$ escape without attenuation. The occultation factor μ_0 is modified for what is effectively a wavelength-dependent stellar size.

The upshot for calculation of line luminosities is that the lower limit for the integration in radius (or the upper limit in terms of inverse radius) is the greater of r_1 and r_0. In the illustrative case of variable mass loss explored in this paper, the emissivity scales as density squared, whereas photoabsorption optical depth is only linear in density, yet the attenuation is exponential in the optical depth. Ultimately, larger values of r_1 tend to drive the line ratio to $R \to R_0$, and additionally depress the strengths of the line emissions and affect the profile shapes.